

**Giant superlinear power dependence of photocurrent
based on layered Ta₂NiS₅ photodetector**

Xianghao Meng^{1,2,†}, Yuhan Du^{1,2,†}, Wenbin Wu^{1,2,†}, Nesta Benno Joseph³, Xing Deng⁴, Jinjin Wang⁴, Jianwen Ma⁵, Zeping Shi^{1,2}, Binglin Liu^{1,2}, Yuanji Ma^{1,2}, Fangyu Yue^{1,2,4}, Ni Zhong^{1,2,4}, Ping-Hua Xiang^{1,2,4}, Cheng Zhang^{5,6}, Chun-Gang Duan^{1,2,4}, Awadhesh Narayan³, Zhenrong Sun^{1,2}, Junhao Chu^{2,4,7}, Xiang Yuan^{1,2*}

¹State Key Laboratory of Precision Spectroscopy, East China Normal University, Shanghai 200241, China

²School of Physics and Electronic Science, East China Normal University, Shanghai 200241, China

³Solid State and Structural Chemistry Unit, Indian Institute of Science, Bangalore 560012, India

⁴Key Laboratory of Polar Materials and Devices, Ministry of Education, East China Normal University, Shanghai 200241, China

⁵State Key Laboratory of Surface Physics and Institute for Nanoelectronic Devices and Quantum Computing, Fudan University, Shanghai 200433, China

⁶Zhangjiang Fudan International Innovation Center, Fudan University, Shanghai 201210, China

⁷Institute of Optoelectronics, Fudan University, Shanghai 200438, China

*Correspondence and requests for materials should be addressed to X. Y. (E-mail: xyuan@lps.ecnu.edu.cn)

†These authors contributed equally to this work.

Giant superlinear power dependence of photocurrent based on layered Ta₂NiS₅ photodetector

Abstract

Photodetector based on two-dimensional (2D) materials is an ongoing quest in optoelectronics. These 2D photodetectors are generally efficient at low illuminating power but suffer severe recombination processes at high power, which results in the sublinear power dependence of photoresponse and lower optoelectronic efficiency. The desirable superlinear photocurrent is mostly achieved by sophisticated 2D heterostructures or device arrays, while 2D materials rarely show intrinsic superlinear photoresponse. Here, we report the giant superlinear power dependence of photocurrent based on multi-layer Ta₂NiS₅. While the fabricated photodetector exhibits good sensitivity (3.1 mS/W per \square) and fast photoresponse (31 μ s) , the bias-, polarization-, and spatial-resolved measurements point to an intrinsic photoconductive mechanism. By increasing the incident power density from 1.5 μ W/ μ m² to 200 μ W/ μ m² , the photocurrent power dependence varies from sublinear to superlinear. At higher illuminating conditions, a prominent superlinearity is observed with a giant power exponent of $\gamma = 1.5$. The unusual photoresponse can be explained by a two-recombination-center model where the distinct density of states of the recombination centers effectively closes all recombination channels. The fabricated photodetector is integrated into camera for taking photos with enhanced contrast due to the superlinearity. Our work provides an effective route to enable higher optoelectronic efficiency at extreme conditions.

Introduction

Optoelectronic devices based on two-dimensional (2D) materials have attracted intense research attention owing to their excellent performances of high sensitivity^{1,2}, fast response time^{3,4}, and high electron mobility^{5,6}. The photoconductive detector is one of the most stable optoelectronic devices with broad working bandwidth⁷, high responsivity⁸, and high gain⁹. The photoresponse of this device is mainly determined by material properties due to the simple structure and physical mechanism. When semiconductor material absorbs incident photons, whose energy is equal to or greater than the bandgap, photon-generated electrons and holes will be separated in opposite directions and collected by the electrodes with an external bias. The photocurrent (I_{ph}) increases as a function of incident power (P) following a power-law dependence of $I_{\text{ph}} \propto P^\gamma$. The power exponent (γ) varies between different materials because of electron-hole generation, trapping, recombination process and other mechanisms¹⁰⁻¹³.

For the ideal case, a linear increase of photocurrent with incident power is expected ($\gamma = 1$) since the photocurrent is solely determined by the photogeneration of electron-hole pairs¹⁴⁻¹⁹. In most 2D-based devices, I_{ph} exhibits a sublinear power dependence under high-intensity illumination due to dominating contribution from defects and impurities. As light intensity increases, those defects serve as effective recombination centers and capture more photocarriers which lead to the saturation of photocurrent ($\gamma < 1$)^{15,20-22} and decreased responsivity. As for superlinear power dependence ($\gamma > 1$), it is found in comparatively rare cases and features increased photoresponsivity with power^{23,24}. Recently, the superlinear power-dependent photocurrent was reported in a series of artificial 2D structures such as graphene/h-BN²⁵, graphene/WSe₂²⁶, WS₂/MoS₂²⁷ heterojunctions, and sheet array²⁸. The typical origin of superlinearity from heterostructure devices is the photothermionic effect, where hot carriers are injected from the gate side to overcome the Schottky barrier exponentially as external injection bias increases, resulting in significantly extended spectral bandwidth and responsivity^{25,26,29}. Meanwhile, the multi-center Shockley-Read-Hall process^{28,30} also contributes to the superlinear response in arrayed structures such as printed MoS₂ and GaTe transistor arrays because the array structure keeps photocarriers from massive recombination at high luminous power³⁰.

The desired superlinear photoresponse is mainly achieved by sophisticated 2D heterostructures and arrays²⁵⁻²⁹. However, as the building block of those 2D artificial structures, the 2D materials rarely show intrinsic superlinear photoresponse. Even within the existing cases, the superlinearity is weak with power-law exponent γ generally lower than 1.1. Hereafter, we define “homogeneous 2D material”³¹ as those single 2D material that contrasts the heterostructures and arrays. Homogeneous 2D material with stronger intrinsic superlinearity (higher γ) is desired which potentially allows for stronger optoelectronic efficiency at the high power regime and enables better performance if integrated into the discussed sophisticated structures.

In this work, we report the prominent and intrinsic superlinear power dependence of photocurrent based on homogeneous Ta₂NiS₅ at ambient condition. The photodetector manifests itself with a simple metal-Ta₂NiS₅-metal structure. Bias-dependent and spatial scanning photocurrent measurements suggest the photoconductive origin of the photoresponse so that the photocurrent is determined by the intrinsic material property of Ta₂NiS₅. The photoconductive devices feature a fast response of 31 μ s, along with good sensitivity of 3.1 mS/W per \square , and polarization-sensitive anisotropy. At the low intensity regime (1.5 – 15 μ W/ μ m²), photocurrent shows conventional sublinear power dependence. Upon increasing the power density (15 – 200 μ W/ μ m²), the photocurrent becomes weakly superlinear. With illuminating power density higher than 200 μ W/ μ m², strong superlinear power dependence is found with a giant power exponent $\gamma = 1.5$ for the homogeneous 2D material. Different from the previous report³² where the capture cross-section plays a major role in determining the weak superlinearity, here, the unusual strong superlinearity requires the presence of recombination centers with distinct density of states. We present a two-recombination-center (RC) model to capture the main finding of the experiments which is further quantitatively proved by the multi-parameter fitting. The fabricated Ta₂NiS₅ device is tested for taking photographs. The image contrast is clearly enhanced due to the superlinearity of the device. Our work sheds light on the superlinear photocurrent which allows enhanced optoelectronic performance of photoconductive devices at high illuminating power.

Ta₂NiS₅ crystallizes in the orthorhombic system (space group Cmcm, D_{2h}¹⁷) as shown

in Fig. 1a, which is composed of layers stacking along b-axis. Each layer consists of the periodically arranged $[\text{TaS}_6]_2$ chains and NiS_4 chains. The armchair structure runs along the a-axis leading to the quasi-one-dimensional structure^{33,34} along with the resultant anisotropic electronic and optical characteristics^{35,36}. The high-quality Ta_2NiS_5 crystals are prepared by chemical vapor transport method (Fig. 1b) with temperature gradient of 6 °C/cm. The needle-like crystals (Fig. 1c) are found in the cold end with shiny surfaces. More details can be found in the *Method* section. As shown in Fig. 1d, the copper target X-ray diffraction (XRD) pattern of the as-grown Ta_2NiS_5 crystal is performed to evaluate the crystal structure and orientation. The prominent peaks at 14.6°, 29.4°, and 44.8° originate from the (010) plane. The extracted lattice constant b is 12.11 Å. The inset presents the full width at half-maximum (FWHM) of 0.16°. The lattice properties and anisotropic characteristics can be further examined by Raman microscope. The randomly polarized Raman spectrum is shown in Fig. 1e which is measured under ambient condition with HeNe laser. Apparent peaks at 127.0 cm^{-1} and 148.6 cm^{-1} correspond to the $^2\text{A}_g$ and $^3\text{A}_g$ phonon modes, respectively³⁷. Angle-resolved polarized Raman spectra are carried out in both parallel and perpendicular polarization configurations. Figure. 1f and Figure. 1g present the false-color maps of the Raman spectra. The original spectra are provided in Supplementary Section II. The experimental coordinate x, y, z coincides with the crystal direction a, b, c , respectively. The excitation beam propagates in y direction and the polarization is controlled by a half-wave plate. More details are provided in the *Method* section and Supplementary Section II. The Raman tensor of A_g modes in Ta_2NiS_5 is given by³⁸

$$\mathbf{R}(\text{A}_g) = \begin{pmatrix} |a|e^{i\varphi_a} & & \\ & |b|e^{i\varphi_b} & \\ & & |c|e^{i\varphi_c} \end{pmatrix} \quad (1)$$

The anisotropic Raman response can be quantitatively derived as

$$I_{\parallel}(\text{A}_g) \propto |c|^2 \left\{ \left(\sin^2\theta + \frac{|a|}{|c|} \cos\varphi_{ca} \cos^2\theta \right)^2 + \left(\frac{|a|}{|c|} \sin\varphi_{ca} \cos^2\theta \right)^2 \right\} \quad (2)$$

$$I_{\perp}(\text{A}_g) \propto \frac{1}{4} (|a|^2 + |c|^2 - 2|ac|\cos\varphi_{ca}) \sin^2 2\theta \quad (3)$$

$a, b,$ and c are the amplitude of Raman tensor elements. The $\varphi_a, \varphi_b,$ and φ_c are the phases of the elements, and $\varphi_{ca} = \varphi_c - \varphi_a$. θ denotes the angle between the polarization vector of incident light \mathbf{e}_i and the a-axis of the crystal³⁹. The angle-dependent phonon intensity can be well fitted by the Raman tensor as shown in Fig. 1h-

k. In the parallel configuration ($\mathbf{e}_i \parallel \mathbf{e}_s$), $I_{\parallel}(A_g)$ reaches the global maximum along the armchair direction and local maximum along the zigzag direction. Meanwhile, both A_g modes present four-fold symmetry in the perpendicular configuration ($\mathbf{e}_i \perp \mathbf{e}_s$). The polarized Raman spectra agree with the theoretical prediction and help to identify the crystal direction. Based on our infrared spectroscopy measurement, a direct band gap of 273 meV is extracted for the as grown Ta_2NiS_5 which agrees with the general consensus of Ta_2NiS_5 being a narrow gap semiconductor^{36,37,40}. More details are given in Supplementary Section VI.

To examine optoelectronic properties of multi-layer Ta_2NiS_5 , the as-grown single crystals are exfoliated by mechanical method, and device fabrications are performed by a home-built lithography system with lift-off procedures. Fig. 2a exhibits the schematic diagram of the device structure. The multi-layer Ta_2NiS_5 is transferred to the SiO_2/Si substrate and contacted by electrodes (5 nm Cr/70 nm Au). The photocurrent is measured under the ambient condition with illumination of 632.8 nm laser. Due to the narrow gap nature of Ta_2NiS_5 ³⁶, the photoresponse is expected to be insensitive to the wavelength of visible lasers, but the laser beam with lower wavelength is found capable of damaging the sample at moderate intensity. Fig. 2b depicts the bias-dependent photocurrent with incident power density $p = 0.324 \text{ mW}/\mu\text{m}^2$ (defined as incident power per unit area). The edge of the spot size is defined by the position with 1.5 standard deviations. The photocurrent I_{ph} is defined as $I_{ph} \equiv I_{illumination} - I_{dark}$, which describes the difference between current with and without laser illumination. The measured photocurrent presents symmetric and linear bias dependence and goes through the origin of the plot. The photocurrent is extracted as $I_{ph} = 5.35 \text{ }\mu\text{A}$ under bias voltage of $U = 1 \text{ V}$ and incident power density of $p = 0.324 \text{ mW}/\mu\text{m}^2$. The photoresponsivity reaches a reasonable value of $R_{\lambda} = \frac{I_{ph}}{p} = 2.5 \text{ mA/W}$ in small-gap semiconductor⁴¹. The R_{λ} does not reflect the intrinsic property of the device and material since it varies with the bias. A more proper physical parameter is the photoconductive responsivity R_{σ} extracted as $3.1 \text{ mS/W per } \square$. Fig. 2c exhibits the dark current which is also symmetric and linear with bias, proving the Ohmic contact of the device as an important prerequisite for high-performance devices³. The observed bias dependence suggests the photoconductive origin rather than the photovoltaic mechanism of the measured device. Otherwise, the Schottky barrier or

other built-in potential results in the nonlinear response in both $I_{\text{dark}} - U$ and $I_{\text{ph}} - U$ test^{24,42,43}. Meanwhile, the negligible photocurrent at $U = 0$ V is also against the photovoltaic mechanism. Fig. 2d is the image of the device, and the scale bar is 10 μm . The height profile (inset) is measured along the white dashed line, suggesting the thickness of 178 nm of Ta_2NiS_5 flake. The photoconductive origin is further proved by spatial-resolved experiments as shown in Fig. 2e. The photocurrent is measured along the red dash line with $U = 1$ V and $p = 0.324$ $\text{mW}/\mu\text{m}^2$. The FWHM of the laser spot is 1.44 μm (Supplementary Section I, Fig. S1), which is much smaller than the size of the sample and ensures the spatial resolution. The blue and green arrows denote edges between the sample and electrodes. It is evident that the photocurrent originates from the sample and vanishes at electrodes which excludes the photothermoelectric effect as well as the Schottky barrier origin.

The optoelectronic property of the photoconductive device is further examined by switching, time-dependent and polarization-dependent experiments. Fig. 2f exhibits the on-off repeatability test where the photoresponse remains identical after 2,000 cycles. The period of each cycle is about 10 s. We periodically block the laser and continuously measure the photocurrent versus time. The response speed of the device is found beyond the limit of the repeatability test system, so we perform a modulation-frequency-dependent study to accurately extract the photoresponse time τ by lock-in technique. The normalized photocurrent at different chopping frequencies is plotted in Fig. 2g. The frequency-dependent photoresponse is expected to follow⁴⁴ $I_{\text{ph}}(\omega)/I_{\text{ph}}(0) = 1/\sqrt{1 + (2\pi\omega\tau)^2}$. The best fitting of the experimental results gives a fast photoresponse time of $\tau = 31.1$ μs . The comparative fast photoresponse suggests finite influence from the dopants. Meanwhile, the Ta_2NiS_5 crystal is known to be anisotropic, and we studied the photoresponse by illuminating the device with linear-polarized light. The angle-dependent photocurrent is shown in Fig. 2h. With the crystal direction verified by angle-resolved Raman spectra, a prominent anisotropic photocurrent is observed with two-fold symmetry which maximizes along the armchair direction.

The photoconductive origin of the photocurrent is evident by the discussed photocurrent measurements with multiple tuning knobs. The photovoltaic and

photothermoelectric mechanisms are firstly ruled out because of the linear bias-dependent and spatial origin. The working frequency of our device also precludes the Dyakonov–Shur mechanism which is usually observed in THz regime^{31,45}. The bolometric mechanism behaves similarly in bias- and spatial-resolved experiments, but the response speed of the Ta₂NiS₅ device is much faster than the general bolometric devices with a typical response time of 1 – 100 ms^{46,47}. In addition, the absorption rate of the Ta₂NiS₅ is found to be independent of the incident light power. Meanwhile, the conductivity of Ta₂NiS₅ increases linearly with temperature. These facts, combined with the observation of superlinear power dependence, further validate that the bolometric effect does not contribute to the observed photoresponse. More details are given in Supplementary Section IV.

In addition to the discussed device performance, an unusual phenomenon is found in the power dependence of the photocurrent. Fig. 3a exhibits $I_{\text{ph}} - U$ curves under different incident light intensities. The incident laser spot is kept at the center of the sample. The higher incident power is expected to result in larger photocurrent due to the increased photogenerated electron-hole pairs in the Ta₂NiS₅. Lower intensity data is not shown because of the overlapping with other low intensity curves. We extract the photocurrent at $U = 1$ V, as exhibited in Fig. 3b. A clear trend of superlinear power dependence is witnessed. As shown in the inset of Fig. 3b, the photoconductivity first declines with the light power and then increases slowly. A drastic rising of R_{σ} is observed at high illumination power, indicating counterintuitive higher optoelectronic efficiency. To better resolve that, we plot the photocurrent in different incident power regimes and perform the power-law fitting in Fig. 3c-e following $I_{\text{ph}} \propto p^{\gamma}$. With incident power density lower than $0.015 \text{ mW}/\mu\text{m}^2$, a sublinear power dependence of the photocurrent is observed with $\gamma = 0.53 \pm 0.03$. The error scale is given by the fitting error. By increasing the illuminating power, the power dependence of the photocurrent experiences a transition from sublinear to superlinear. Within the power regime of $0.015 - 0.2 \text{ mW}/\mu\text{m}^2$, the photocurrent becomes weakly superlinear with $\gamma = 1.15 \pm 0.01$. As light intensity further increases, strong superlinear dependence is found at the high incident power regime with the power exponent of $\gamma = 1.5 \pm 0.1$. A similar trend can also be found in the linear fit of log-log plot (Supplementary Section III). To the best knowledge of the authors, such strong superlinearity is unusual for

homogeneous 2D materials. As summarized in Fig. 3f, the superlinear response of homogeneous 2D devices is generally weak with γ value lower than 1.1^{11,23,32,48}. Our result of $\gamma = 1.5$ represents a giant superlinearity of the photocurrent in Ta₂NiS₅ device which enables higher optoelectronic efficiency at high incident power. The x -axis is sorted in the order of report time.

To explain the superlinear dependence of the photocurrent under high incident power, we provide a two-recombination-center (RC) model as illustrated in Fig. 4. Different from previous reports^{11,23,49–51} where three centers are required, we will discuss later that the two-RC model is more suitable for narrow gap Ta₂NiS₅. The VB and CB denote valence band and conduction band, respectively. Besides, there might also exist a few in-gap states. The presence of those in-gap states is also evidenced by our infrared spectroscopy measurements as discussed in detail in Supplementary Section VI. Our density functional calculation (DFT) suggests that one of the in-gap states might originate from the S vacancy. The in-gap states might also result from other defects such as impurities and dangling bonds^{49,52–54} (More details in Supplementary Section VII). These in-gap states act as recombination centers of the photogenerated carriers which could significantly reduce the quantum efficiency. Based on our infrared and transport results, the dopants are at least partially ionized (Supplementary Section VIII). To account for the superlinearity, those two recombination centers (RC_{*i*}, *i*=1,2) feature distinct parameters. Among them, the most critical two are the density of states (N_i) and the capture cross-sections for electrons (S_{n_i}). S_{n_i} describes the ability of RC_{*i*} to capture the electron. Considering the described system at equilibrium, upon absorbing incident photons, electron-hole pairs are generated across the band gap (process A). The solid and hollow dots denote electrons and holes, respectively. Before those carriers are collected by the electrodes, there is a certain probability (mainly determined by S_{n_i}) for the photogenerated electrons to be captured by RC₁ (process B) or RC₂ (process C). Similarly, RC might also capture the photogenerated holes from valence band (process E & G). Meanwhile, it is possible for the captured electron on RC₂ to be thermally emitted to the conduction band (process D) before recombined with holes, while the captured holes might experience the similar procedure (process F). All those procedures influence the carrier population of the states and in turn vary the probability of each procedure. The probability between different processes varies dramatically with

different orders of magnitude. For example, the cross-sections of process B, E, H (labeled in dashed line) are negligibly low due to the large energy difference between initial and final states. All processes are considered in the model calculation despite its probability. It is worth to note that process A is the only one originating from the photoelectric transition. All remaining processes denote pure electric processes including thermal excitation, trapping, and nonradiative recombination. Other photoelectric transitions and occupation conditions are further discussed in Supplementary Section V. Based on the modulation frequency dependent measurement, all those procedures and resultant carrier population reaches equilibrium within hundred μ s. Owing to the orders of magnitude higher capture rate for hole, the photocurrent is dominated by carrier concentration of photogenerated electron n in the conduction band^{13,24}. Therefore, the photocurrent reads as $I_{ph} = nq\mu ES$, where q is electronic charge, μ is mobility, E is electric field, and S is cross-sectional area of the channel¹⁹. Without light illumination, the Fermi level in our model lies near the center of gap. This is further supported by the excitation energy extracted by the transport measurement (Details given in Supplementary Section VIII). The Fermi level may stay close to the gap center but deviate a few meV. As a result, RC₁ is almost filled and RC₂ is nearly empty because of finite thermal excitation. By applying incident light, process C and G are significantly enhanced. Therefore, as reaching the equilibrium shown in Fig. 4a, the RC₂ becomes more occupied but most of the states remain empty. Meanwhile, RC₁ is less occupied. With higher incident power as depicted in Fig. 4b, the photogenerated carriers lead to the higher occupation rate of RC₂ and lower occupation for RC₁ which now qualitatively varies the system behavior. The occupation condition influences the strength of all the discussed process A-H.

The response of the photoconductive device can be analyzed by the proposed model. In the upper panel of Fig. 5a, we first consider the conventional case where the properties of RC₁ and RC₂ are similar. Since the photocurrent is determined by electron concentration, we focus on electron-related processes. Both RC₁ and RC₂ provide efficient recombination channels through process B and process C, resulting in the recombination of photogenerated carriers before being collected by electrodes. The recombination rate increases with incident power, which in general case, saturates the photocurrent. Therefore, the photocurrent is expected to be linear or sublinear on the

power dependence, as exhibited in the lower panel. As suggested by previous work¹³, different capture cross-sections of the RC potentially lead to weak superlinear dependence of the photocurrent. If the electron capture cross-section of RC₁ (S_{n_1}) is much smaller than RC₂ (S_{n_2}), the recombination channel on the RC₁ is effectively closed (denoted by red crossings in Fig. 5b) and most of the photogenerated electron is trapped by RC₂. At high incident power regime, the RC₂ becomes densely occupied, which suppresses the process C as denoted by dashed line. Lower recombination rate at higher intensity allows for higher optoelectronic efficiency and leads to the superlinear behavior of the power dependence. To account for the observed giant superlinear photoresponse, another critical parameter N_i is taken into consideration. With much lower density of states of RC₂ shown in Fig. 5c, the occupation condition qualitatively varies at high incident power. Since the density of states of RC₂ is much lower, higher incident light leads to the rapid saturation of RC₂ which forbids the C process as well as the recombination channel on RC₂. Combined with negligible S_{n_1} , now both of the recombination channels are closed at the high power regime. Therefore, a giant superlinear power dependence is presented as shown in the lower panel.

To elucidate the effects of N_1/N_2 on superlinear photocurrent, we perform the numerical calculation based on the two-RC model. For each energy level in this model, all related carrier procedures reach equilibrium in the end. For example, the photogenerated electron concentration of the conduction band is given by

$$\frac{dn}{dt} = F - n[vS_{n_1}(N_1 - n_1) + vS_{n_2}(N_2 - n_2)] + n_2P_2 - S'vnp = 0 \quad (4)$$

The F , $-nvS_{n_1}(N_1 - n_1)$, $-nvS_{n_2}(N_2 - n_2)$, n_2P_2 , and $-S'vnp$ term corresponds to the procedure A, B, C, D, and H, respectively; n, n_1, n_2 represents the electron density of conduction band, RC₁, and RC₂, respectively; p represents the hole density of valence band; v denotes thermal velocity of the carriers which is assumed to be equal for simplicity; F denotes the density of electron-hole pairs created by optical excitation per second which is determined by light intensity, quantum efficiency, and absorption rate; S_{n_1}, S_{n_2} denotes the electron capture cross-section of RC₁ and RC₂, respectively; S' denotes recombination cross-section between free electrons and free holes; P_2 denotes the probability per unit time for the thermal ejection of an electron in RC₂ into the CB. For all other energy levels, similar equations can be derived

by fully considering related carrier procedures which ultimately achieve equilibrium. The overall equations are provided in Supplementary Section V. By solving the nonlinear equations, the photoresponse of the device with different parameter settings can be numerically extracted. Fig. 5d depicts the occupation proportion of RC₂. For parameter settings with high N_1/N_2 (green curve), the electron concentration is intensely saturated at high incident power. In contrast, such a saturation feature is weakened for lower values setting of N_1/N_2 . The difference in the electron density has a profound influence on the electron density of conduction band through process C and process D. This is further supported by the calculated photocurrent in Fig. 5e. Regardless of the N_1/N_2 setting, all curves exhibit a superlinear feature due to the negligible S_{n_1} . However, a higher N_1/N_2 leads to a more prominent superlinear power dependence of the photocurrent which agrees with the discussed picture.

To quantitatively verify the proposed model, we perform the multi-parameter fitting as shown in Fig. 5f. Due to the nonlinearity of the equation, the fitting is carried out using gradient descent method which reaches convergence within 1 day. The experimental available values, such as the gap size, are fixed. The black dots denote experimental data of the Ta₂NiS₅ device which is well-fitted by the model (red line). The critical fitting parameters are extracted as $N_1/N_2 = 16.06$, $S_{n_1}/S_{n_2} = 0.87 \times 10^{-4}$ (more details are provided in Supplementary Section V). It is worth noting that the experimental data can be fitted by both two-RC and three-RC models with qualitative similarity. Thus, the two-RC model is introduced for simplicity which also avoids possible overfitting. Here the fitted model describes a small gap semiconductor system in agreement with our infrared spectroscopy result and the generally accepted picture^{35,36,55}. Further wavelength-dependent research, especially in the mid-infrared regime, might give new insights into both band information and photoresponse.

The observed fast photoresponse speed also agrees with the proposed model. The superlinear photocurrent requires the presence of recombination centers. However, the strong superlinearity also requires the dopant density as well as the density of states for the in-gap states to be low. Only with low dopant density, the recombination center can be fully occupied at high illuminating power. Otherwise, superlinearity is not expected to be observed. The fast photoresponse speed is further contributed by the suppression

of the recombination process under light illumination. While lowering the power, the response speed of the device drops as discussed in detail in Supplementary Section IX. As a result of superlinearity, the photocurrent is also expected to drop while expanding the laser spot. The deduction has been confirmed in our beam-size-dependent experiments as discussed in detail of Supplementary Section X.

To test the Ta₂NiS₅ photodetector and observed superlinearity for potential applications, the imaging function of the device is evaluated. The fabricated device is transferred to the image plane of a camera and controlled by a translation stage so that it mimics the CCD of the camera after a complete scanning. A screen showing the image of an apple is used as the target with tunable brightness. The photos are exhibited in Fig. 6a with 100 ms exposure time where the apple is successfully photographed. With higher brightness of the target, the apple becomes more distinguishable and can be observed in more detail. For more quantitative analysis, root mean square (RMS) contrast of the image is extracted with the definition

$$\text{RMS contrast} = \sqrt{\frac{1}{MN} \sum_{i=0}^{M-1} \sum_{j=0}^{N-1} (I_{phij} - \bar{I}_{ph})^2}, \quad (5)$$

where M and N are the number of pixels per row and per column, respectively. \bar{I}_{ph} is the average value of the signal. As shown in Figure. 6b, the RMS contrasts of the image increase with the maximum detected power among all pixels. Notably, a superlinear trend is found, resembling superlinear photoconductivity. By supporting better imaging contrast, superlinear photodetector could be promising for future optoelectronic detection.

The recombination center plays an important role in the superlinearity photoresponse. More sophisticated experimental tools and theoretical calculations might help to identify the origin of the in-gap states and extract their evolution upon light illumination for better understanding of the system.

In summary, we report the optoelectronic characteristics of the photoconductive detector based on multi-layer Ta₂NiS₅ and discover a giant superlinear power dependence of photocurrent. The time-resolved, frequency-resolved, spatial-resolved,

bias-resolved, and angle-resolved photocurrent measurements not only present a fast, enduring, and anisotropic photoresponse, but also suggest the photoconductive nature of the device which ensures that the device performance is determined by the material property of Ta₂NiS₅. Starting from illumination power density of 1.54 μW/μm², photocurrent presents a sublinear photocurrent with the power density. Around 15.4 μW/μm², a transition from sublinearity to superlinearity is witnessed. With incident power density higher than 0.2 mW/μm², a prominent superlinearity is observed with power exponent $\gamma = 1.5$. The strong superlinearity can be quantitatively explained by a two-RC model. The in-gap recombination centers with distinct density of states and capture cross-sections lead to the rapid saturation of carrier occupancy, thereby, both recombination channels are closed and enable higher optoelectronic efficiency at large incident power. The quantitative fitting between the proposed model and experiments further validates the proposed physical mechanism. The photos taken by the Ta₂NiS₅ demonstrate enhanced RMS contrast showing potential applications of the superlinear photocurrent. Our work paves the way for the superlinearity of optoelectronic devices and enables better device performance in high-power applications.

Methods

Crystal growth and characteristic

Ta₂NiS₅ single crystals were prepared by standard chemical vapor transport method. Stoichiometric mixture of Ta, Ni, and S powder was sealed in a 20 cm vacuum quartz tube with iodine as transport agent. The tube was loaded in a two-zone furnace kept at 950 °C and 830 °C. After a 5-day growth procedure, shiny and needle-like single crystals were found in the low-temperature zone. X-ray diffraction was tested by Bruker D8 Discover. Raman spectrum was tested by a home-built system using 632.8 nm laser.

Device fabrication

Multi-layer Ta₂NiS₅ flakes were mechanically exfoliated from bulk crystals and then transferred to a Si/SiO₂ wafer. Devices were fabricated by self-made lithography system with lift-off procedures. Cr/Au (5 nm/70 nm) is deposited as electrodes and Ohmic contact has been proved by the $I - U$ measurement.

Photocurrent measurement

Photodetectors were excited by 632.8 nm laser through a 50 \times , NA = 0.8 objective. The FWHM of the focal spot is 1.44 μ m. Bias-, angle-, spatial-, time- and power-dependent photocurrent were measured by Keithley 2450 using two-terminal method. Spatial photocurrent scanning was carried out by an additional piezo-actuated stage. The photoswitching test was performed with a periodically switched shutter. The modulation frequency-dependent measurement was carried out by Stanford Research SR-860 lock-in amplifier with a chopper.

Supporting Information

Supplementary information is available from the Wiley Online Library or from the author.

Acknowledgements

We gratefully thank T.-Y. Zhai, L.-J. Li, Q.-J. Wang, J.-B. Li, Y.-Z. Zhang, and L. Li for helpful suggestions on the superlinearity photocurrent and experiments. X.Y. was supported by the National Natural Science Foundation of China (grant no. 62005079 and no. 12174104), the Shanghai Sailing Program (grant no. 20YF1411700), the International Scientific and Technological Cooperation Project of Shanghai (grant no. 20520710900) and a start-up grant from East China Normal University. C.Z. was supported by the National Natural Science Foundation of China (grant no. 12174069), Shanghai Sailing Program (grant no. 20YF1402300), Natural Science Foundation of Shanghai (grant no. 20ZR1407500), the Young Scientist project of the Ministry of Education innovation platform and a start-up grant from Fudan University. NBJ was supported by the Prime Ministers Research Fellowship. A.N. thanks the Indian Institute of Science for a startup grant. C.D. and F.Y. acknowledge the support from the National Key Research Project (grant 2022YFA1402902) and the National Natural Science Foundation of China (grant 62274061).

Conflict of Interest

The authors declare no conflict of interest.

Author contributions

X.Y. conceived the idea and supervised the overall research. X.M. carried out the growth of the Ta₂NiS₅ single crystals; J.M. and Y.D. performed the crystal

characterization including XRD and infrared spectrum with help from W.W. and Z.S. under the supervision of C.Z., C.D. and Z.S.; X.D., J.W., B.L., and Y.M. conducted the device fabrication under the supervision of F.Y., N.Z., P.X., and C.D.; X.M. conducted the photocurrent experiments with help from Y.D. and Z.S.; N.J. performed the DFT calculation under the supervision of A.N.; X.Y., X.M., Y.D., C.Z., and J.C. wrote the paper with the help of all authors.

Data availability statement

The data that support the findings of this study are available from the corresponding author upon reasonable request.

Keywords

layered ternary chalcogenides, superlinear photoresponse, photoconductive detector, high power sensor

References

1. Yin, J., Tan, Z., Hong, H., Wu, J., Yuan, H., Liu, Y., Chen, C., Tan, C., Yao, F., Li, T., Chen, Y., Liu, Z., Liu, K. & Peng, H. Ultrafast and highly sensitive infrared photodetectors based on two-dimensional oxyselenide crystals. *Nature Communications* **9**, 3311 (2018).
2. Lopez-Sanchez, O., Lembke, D., Kayci, M., Radenovic, A. & Kis, A. Ultrasensitive photodetectors based on monolayer MoS₂. *Nature Nanotechnology* **8**, 497–501 (2013).
3. Yuan, X., Tang, L., Liu, S., Wang, P., Chen, Z., Zhang, C., Liu, Y., Wang, W., Zou, Y., Liu, C., Guo, N., Zou, J., Zhou, P., Hu, W. & Xiu, F. Arrayed van der Waals Vertical Heterostructures Based on 2D GaSe Grown by Molecular Beam Epitaxy. *Nano Letters* **15**, 3571–3577 (2015).
4. Jacobs-Gedrim, R. B., Shanmugam, M., Jain, N., Durcan, C. A., Murphy, M. T., Murray, T. M., Matyi, R. J., Moore, R. L. & Yu, B. Extraordinary Photoresponse in Two-Dimensional In₂Se₃ Nanosheets. *ACS Nano* **8**, 514–521 (2014).
5. Bandurin, D. A., Tyurnina, A. V., Yu, G. L., Mishchenko, A., Zólyomi, V., Morozov, S. V., Kumar, R. K., Gorbachev, R. V., Kudrynskiy, Z. R., Pezzini, S., Kovalyuk, Z. D., Zeitler, U., Novoselov, K. S., Patané, A., Eaves, L., Grigorieva, I. V., Fal'ko, V. I., Geim, A. K. & Cao, Y. High electron mobility, quantum Hall effect and anomalous optical response in atomically thin InSe. *Nature Nanotechnology* **12**, 223–227 (2017).
6. Zhao, Y., Qiao, J., Yu, Z., Yu, P., Xu, K., Lau, S. P., Zhou, W., Liu, Z., Wang, X., Ji, W. & Chai, Y. High-Electron-Mobility and Air-Stable 2D Layered PtSe₂ FETs. *Advanced Materials* **29**, 1604230 (2017).
7. Dong, R., Bi, C., Dong, Q., Guo, F., Yuan, Y., Fang, Y., Xiao, Z. & Huang, J. An Ultraviolet-to-NIR Broad Spectral Nanocomposite Photodetector with Gain. *Advanced Optical Materials* **2**, 549–554 (2014).
8. Guo, F., Yang, B., Yuan, Y., Xiao, Z., Dong, Q., Bi, Y. & Huang, J. A nanocomposite ultraviolet photodetector based on interfacial trap-controlled charge injection. *Nature Nanotechnology* **7**, 798–802 (2012).
9. Shen, L., Fang, Y., Wei, H., Yuan, Y. & Huang, J. A Highly Sensitive Narrowband Nanocomposite Photodetector with Gain. *Advanced Materials* **28**, 2043–2048 (2016).
10. Gabor, N. M., Zhong, Z., Bosnick, K., Park, J. & McEuen, P. L. Extremely Efficient Multiple Electron-Hole Pair Generation in Carbon Nanotube Photodiodes. *Science* **325**, 1367–1371 (2009).
11. Zhang, B. Y., Liu, T., Meng, B., Li, X., Liang, G., Hu, X. & Wang, Q. J. Broadband high photoresponse from pure monolayer graphene photodetector. *Nature Communications* **4**, 1811 (2013).
12. Albert, R. *Concepts in photoconductivity and allied problems*. (Krieger, 1978).
13. Bube, R. H. Analysis of photoconductivity applied to cadmium-sulfide-type photoconductors. *Journal of Physics and Chemistry of Solids* **1**, 234–248 (1957).

14. Huang, W., Gan, L., Yang, H., Zhou, N., Wang, R., Wu, W., Li, H., Ma, Y., Zeng, H. & Zhai, T. Controlled Synthesis of Ultrathin 2D β -In₂S₃ with Broadband Photoresponse by Chemical Vapor Deposition. *Advanced Functional Materials* **27**, 1702448 (2017).
15. Greca, L. G., Lehtonen, J., Tardy, B. L., Guo, J. & Rojas, O. J. Biofabrication of multifunctional nanocellulosic 3D structures: a facile and customizable route. *Materials Horizons* **5**, 408–415 (2018).
16. Hong, N., Chu, R. J., Kang, S. S., Ryu, G., Han, J.-H., Yu, K. J., Jung, D. & Choi, W. J. Flexible GaAs photodetector arrays hetero-epitaxially grown on GaP/Si for a low-cost III-V wearable photonics platform. *Optics Express* **28**, 36559 (2020).
17. Lei, S., Ge, L., Najmaei, S., George, A., Koppera, R., Lou, J., Chhowalla, M., Yamaguchi, H., Gupta, G., Vajtai, R., Mohite, A. D. & Ajayan, P. M. Evolution of the Electronic Band Structure and Efficient Photo-Detection in Atomic Layers of InSe. *ACS Nano* **8**, 1263–1272 (2014).
18. Zhang, Y., Yu, W., Li, J., Chen, J., Dong, Z., Xie, L., Li, C., Shi, X., Guo, W., Lin, S., Mokkaapati, S. & Zhang, K. Ultra-broadband photodetection based on two-dimensional layered Ta₂NiSe₅ with strong anisotropy and high responsivity. *Materials & Design* **208**, 109894 (2021).
19. Yin, Z., Li, H., Li, H., Jiang, L., Shi, Y., Sun, Y., Lu, G., Zhang, Q., Chen, X. & Zhang, H. Single-Layer MoS₂ Phototransistors. *ACS Nano* **6**, 74–80 (2012).
20. Irkhin, P., Najafov, H. & Podzorov, V. Steady-state photoconductivity and multi-particle interactions in high-mobility organic semiconductors. *Scientific Reports* **5**, 15323 (2015).
21. Zeng, L., Tao, L., Tang, C., Zhou, B., Long, H., Chai, Y., Lau, S. P. & Tsang, Y. H. High-responsivity UV-Vis Photodetector Based on Transferable WS₂ Film Deposited by Magnetron Sputtering. *Scientific Reports* **6**, 20343 (2016).
22. Luo, W., Cao, Y., Hu, P., Cai, K., Feng, Q., Yan, F., Yan, T., Zhang, X. & Wang, K. Gate Tuning of High-Performance InSe-Based Photodetectors Using Graphene Electrodes. *Advanced Optical Materials* **3**, 1418–1423 (2015).
23. Li, L., Wang, W., Gan, L., Zhou, N., Zhu, X., Zhang, Q., Li, H., Tian, M. & Zhai, T. Ternary Ta₂NiSe₅ Flakes for a High-Performance Infrared Photodetector. *Advanced Functional Materials* **26**, 8281–8289 (2016).
24. Klee, V., Preciado, E., Barroso, D., Nguyen, A. E., Lee, C., Erickson, K. J., Triplett, M., Davis, B., Lu, I.-H., Bobek, S., McKinley, J., Martinez, J. P., Mann, J., Talin, A. A., Bartels, L. & Léonard, F. Superlinear Composition-Dependent Photocurrent in CVD-Grown Monolayer MoS_{2(1-x)}Se_{2x} Alloy Devices. *Nano Letters* **15**, 2612–2619 (2015).
25. Kim, Y. R., Phan, T. L., Shin, Y. S., Kang, W. T., Won, U. Y., Lee, I., Kim, J. E., Kim, K., Lee, Y. H. & Yu, W. J. Unveiling the Hot Carrier Distribution in Vertical Graphene/h-BN/Au van der Waals Heterostructures for High-Performance Photodetector. *ACS Applied Materials & Interfaces* **12**, 10772–10780 (2020).
26. Massicotte, M., Schmidt, P., Vialla, F., Watanabe, K., Taniguchi, T., Tielrooij, K. J.

- & Koppens, F. H. L. Photo-thermionic effect in vertical graphene heterostructures. *Nature Communications* **7**, 12174 (2016).
27. Wang, L., Yue, Q., Pei, C., Fan, H., Dai, J., Huang, X., Li, H. & Huang, W. Scrolling bilayer WS₂/MoS₂ heterostructures for high-performance photo-detection. *Nano Research* **13**, 959–966 (2020).
 28. Seo, J.-W. T., Zhu, J., Sangwan, V. K., Secor, E. B., Wallace, S. G. & Hersam, M. C. Fully Inkjet-Printed, Mechanically Flexible MoS₂ Nanosheet Photodetectors. *ACS Applied Materials & Interfaces* **11**, 5675–5681 (2019).
 29. Liu, W., Lv, J., Peng, L., Guo, H., Liu, C., Liu, Y., Li, W., Li, L., Liu, L., Wang, P., Bodepudi, S. C., Shehzad, K., Hu, G., Liu, K., Sun, Z., Hasan, T., Xu, Y., Wang, X., Gao, C., Yu, B. & Duan, X. Graphene charge-injection photodetectors. *Nature Electronics* **5**, 281–288 (2022).
 30. Kang, J., Sangwan, V. K., Lee, H.-S., Liu, X. & Hersam, M. C. Solution-Processed Layered Gallium Telluride Thin-Film Photodetectors. *ACS Photonics* **5**, 3996–4002 (2018).
 31. Koppens, F. H. L., Mueller, T., Avouris, Ph., Ferrari, A. C., Vitiello, M. S. & Polini, M. Photodetectors based on graphene, other two-dimensional materials and hybrid systems. *Nature Nanotechnology* **9**, 780–793 (2014).
 32. Zhang, W., Huang, J.-K., Chen, C.-H., Chang, Y.-H., Cheng, Y.-J. & Li, L.-J. High-Gain Phototransistors Based on a CVD MoS₂ Monolayer. *Advanced Materials* **25**, 3456–3461 (2013).
 33. Sunshine, S. A. & Ibers, J. A. Structure and physical properties of the new layered ternary chalcogenides tantalum nickel sulfide (Ta₂NiS₅) and tantalum nickel selenide (Ta₂NiSe₅). *Inorganic Chemistry* **24**, 3611–3614 (1985).
 34. Di Salvo, F. J., Chen, C. H., Fleming, R. M., Waszczak, J. V., Dunn, R. G., Sunshine, S. A. & Ibers, J. A. Physical and structural properties of the new layered compounds Ta₂NiS₅ and Ta₂NiSe₅. *Journal of the Less Common Metals* **116**, 51–61 (1986).
 35. Sugimoto, K., Nishimoto, S., Kaneko, T. & Ohta, Y. Strong Coupling Nature of the Excitonic Insulator State in Ta₂NiSe₅. *Physical Review Letters* **120**, 247602 (2018).
 36. Larkin, T. I., Yaresko, A. N., Pröpper, D., Kikoin, K. A., Lu, Y. F., Takayama, T., Mathis, Y.-L., Rost, A. W., Takagi, H., Keimer, B. & Boris, A. V. Giant exciton Fano resonance in quasi-one-dimensional Ta₂NiSe₅. *Physical Review B* **95**, 195144 (2017).
 37. Li, L., Gong, P., Wang, W., Deng, B., Pi, L., Yu, J., Zhou, X., Shi, X., Li, H. & Zhai, T. Strong In-Plane Anisotropies of Optical and Electrical Response in Layered Dimetal Chalcogenide. *ACS Nano* **11**, 10264–10272 (2017).
 38. Kranert, C., Sturm, C., Schmidt-Grund, R. & Grundmann, M. Raman tensor elements of β-Ga₂O₃. *Scientific Reports* **6**, 35964 (2016).
 39. Du, Y., Chen, J., Wu, W., Shi, Z., Meng, X., Zhang, C., Gong, S., Chu, J. & Yuan, X. Comparative Raman spectroscopy of magnetic topological material EuCd₂X₂ (X = P, As). *Journal of Physics: Condensed Matter* **34**, 224001 (2022).
 40. Windgätter, L., Rösner, M., Mazza, G., Hübener, H., Georges, A., Millis, A. J.,

- Latini, S. & Rubio, A. Common microscopic origin of the phase transitions in Ta_2NiS_5 and the excitonic insulator candidate Ta_2NiSe_5 . *npj Computational Materials* **7**, 210 (2021).
41. Buscema, M., Island, J. O., Groenendijk, D. J., Blanter, S. I., Steele, G. A., van der Zant, H. S. J. & Castellanos-Gomez, A. Photocurrent generation with two-dimensional van der Waals semiconductors. *Chemical Society Reviews* **44**, 3691–3718 (2015).
 42. Georgiou, T., Jalil, R., Belle, B. D., Britnell, L., Gorbachev, R. V., Morozov, S. V., Kim, Y.-J., Gholinia, A., Haigh, S. J., Makarovskiy, O., Eaves, L., Ponomarenko, L. A., Geim, A. K., Novoselov, K. S. & Mishchenko, A. Vertical field-effect transistor based on graphene– WS_2 heterostructures for flexible and transparent electronics. *Nature Nanotechnology* **8**, 100–103 (2013).
 43. Miao, J., Hu, W., Guo, N., Lu, Z., Liu, X., Liao, L., Chen, P., Jiang, T., Wu, S., Ho, J. C., Wang, L., Chen, X. & Lu, W. High-Responsivity Graphene/InAs Nanowire Heterojunction Near-Infrared Photodetectors with Distinct Photocurrent On/Off Ratios. *Small* **11**, 936–942 (2015).
 44. Lai, J., Liu, X., Ma, J., Wang, Q., Zhang, K., Ren, X., Liu, Y., Gu, Q., Zhuo, X., Lu, W., Wu, Y., Li, Y., Feng, J., Zhou, S., Chen, J.-H. & Sun, D. Anisotropic Broadband Photoresponse of Layered Type-II Weyl Semimetal MoTe_2 . *Advanced Materials* **30**, 1707152 (2018).
 45. Dyakonov, M. & Shur, M. Detection, mixing, and frequency multiplication of terahertz radiation by two-dimensional electronic fluid. *IEEE Transactions on Electron Devices* **43**, 380–387 (1996).
 46. Jiang, W., Zheng, T., Wu, B., Jiao, H., Wang, X., Chen, Y., Zhang, X., Peng, M., Wang, H., Lin, T., Shen, H., Ge, J., Hu, W., Xu, X., Meng, X., Chu, J. & Wang, J. A versatile photodetector assisted by photovoltaic and bolometric effects. *Light: Science & Applications* **9**, 160 (2020).
 47. Itkis, M. E., Borondics, F., Yu, A. & Haddon, R. C. Bolometric Infrared Photoresponse of Suspended Single-Walled Carbon Nanotube Films. *Science* **312**, 413–416 (2006).
 48. Fan, C., Yue, Q., Yang, J., Wei, Z., Yang, S. & Li, J. Low temperature electrical and photo-responsive properties of MoSe_2 . *Applied Physics Letters* **104**, 202105 (2014).
 49. Kushwaha, N., Kushwaha, V. S., Shukla, R. K. & Kumar, A. Determination of energy of defect centres in a- $\text{Se}_{78}\text{Ge}_{22}$ thin films. *Philosophical Magazine Letters* **86**, 691–697 (2006).
 50. Peters, J. A., Cho, N. K., Liu, Z., Wessels, B. W., Li, H., Androulakis, J. & Kanatzidis, M. G. Investigation of defect levels in $\text{Cs}_2\text{Hg}_6\text{S}_7$ single crystals by photoconductivity and photoluminescence spectroscopies. *Journal of Applied Physics* **112**, 063702 (2012).
 51. Anomalous Photoconductive Transport Properties of As_2Se_3 Films. *Egyptian Journal of Solids* **25**, 13–21 (2002).
 52. Jasenek, A. & Rau, U. Defect generation in $\text{Cu}(\text{In,Ga})\text{Se}_2$ heterojunction solar cells

- by high-energy electron and proton irradiation. *Journal of Applied Physics* **90**, 650–658 (2001).
53. Massé, G. & Redjai, E. Radiative recombination and shallow centers in CuInSe₂. *Journal of Applied Physics* **56**, 1154–1159 (1984).
 54. Li, J., Yuan, Z.-K., Chen, S., Gong, X.-G. & Wei, S.-H. Effective and Noneffective Recombination Center Defects in Cu₂ZnSnS₄: Significant Difference in Carrier Capture Cross Sections. *Chemistry of Materials* **31**, 826–833 (2019).
 55. Lu, Y. F., Kono, H., Larkin, T. I., Rost, A. W., Takayama, T., Boris, A. V., Keimer, B. & Takagi, H. Zero-gap semiconductor to excitonic insulator transition in Ta₂NiSe₅. *Nature Communications* **8**, 14408 (2017).

Figures

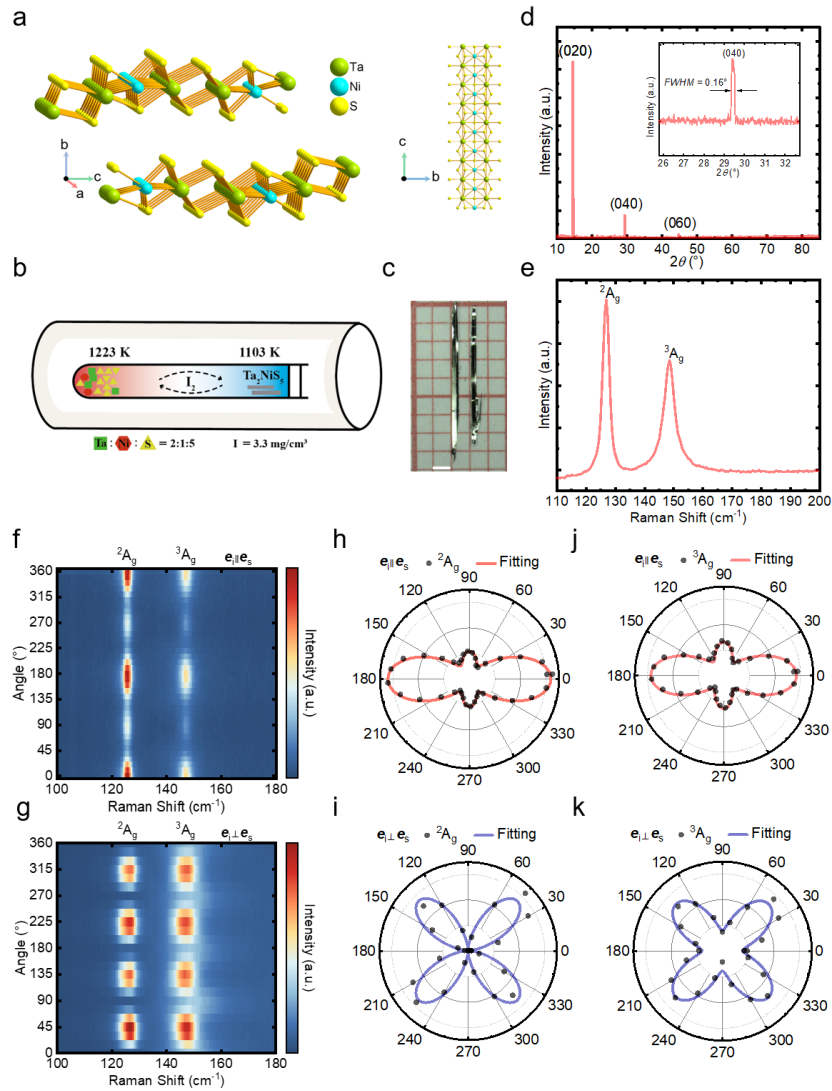


Fig. 1 | X-ray and Raman spectrum of Ta₂NiS₅ single crystals. **a**, The crystal structure of Ta₂NiS₅. **b**, Schematic diagram of the chemical vapor transport process. **c**, The photo of the as-grown single crystal. The scale bar is 1 mm. **d**, X-ray diffraction pattern of Ta₂NiS₅. **e**, Raman spectrum of Ta₂NiS₅ with random polarization. **f-k**, False-color maps and corresponding intensity fittings of the polarization-dependent Raman spectra in parallel and perpendicular configurations.

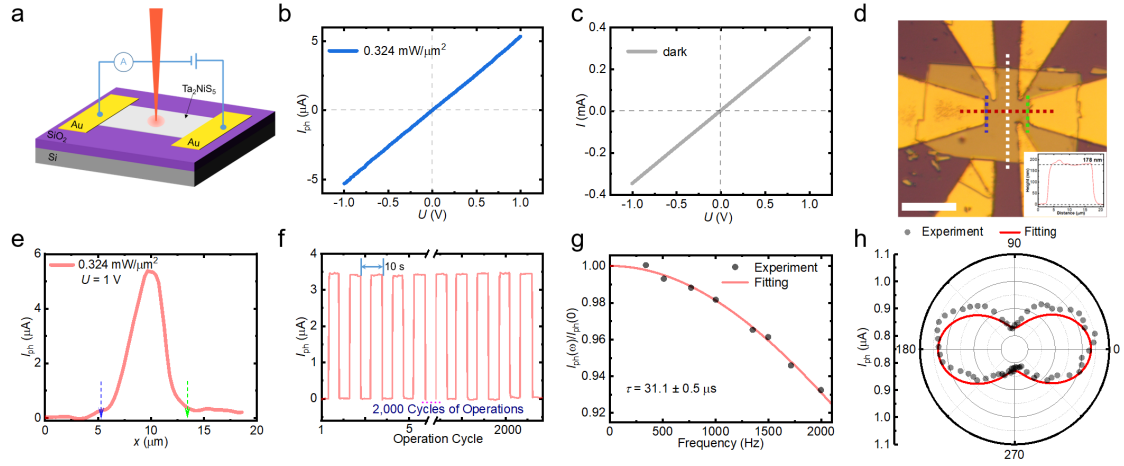


Fig. 2 | Photoconductive origin and performance of the photodetector. **a**, Schematic diagram of the optoelectronic device structure based on exfoliated Ta₂NiS₅. **b**, Linear bias dependence of the photocurrent. **c**, Linear dark current which suggests Ohmic contact of the device. **d**, The photo of the device. The scale bar is 10 μm. The inset exhibits the height profile of the sample (measured along the white dashed line). **e**, Photocurrent profile taken along the red dashed line in **d**. The blue and green arrows denote the edges between the sample and the electrode. **f**, Photoswitching test. **g**, Frequency-dependent photocurrent measurement of the Ta₂NiS₅ device. The fitted response time is $\tau = 31.1 \pm 0.5 \mu\text{s}$. **h**, Polarization-dependent photocurrent of the Ta₂NiS₅ device.

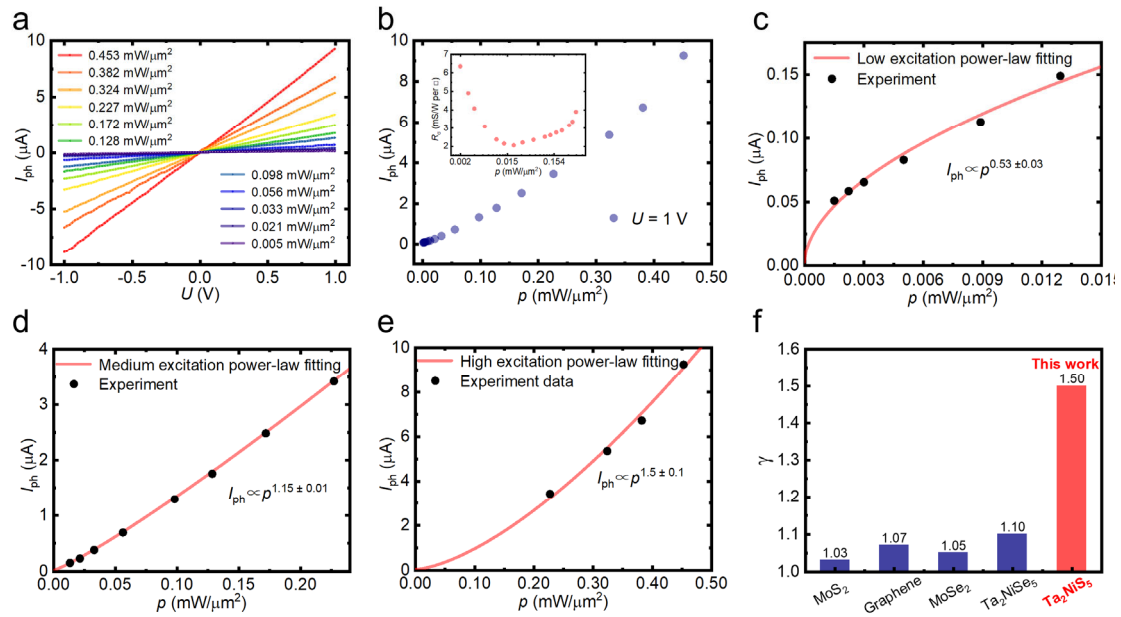


Fig. 3 | Superlinear power dependence of photocurrent. **a**, $I_{ph} - U$ curves of the device under different illuminating power. **b**, The photocurrent extracted at 1 V bias. The inset is the R_σ with a counterintuitive V-shape. Most of the reported optoelectronic devices exhibited a monotonical decrease. **c-e**, The photocurrent and power law fitting at different incident power regimes. The power dependence varies from sublinear at low intensity to superlinear at high intensity. The $\gamma = 1.5$ is reached after $0.2 \text{ mW}/\mu\text{m}^2$. **f**, A comparison of superlinear power exponent among various homogeneous 2D devices.

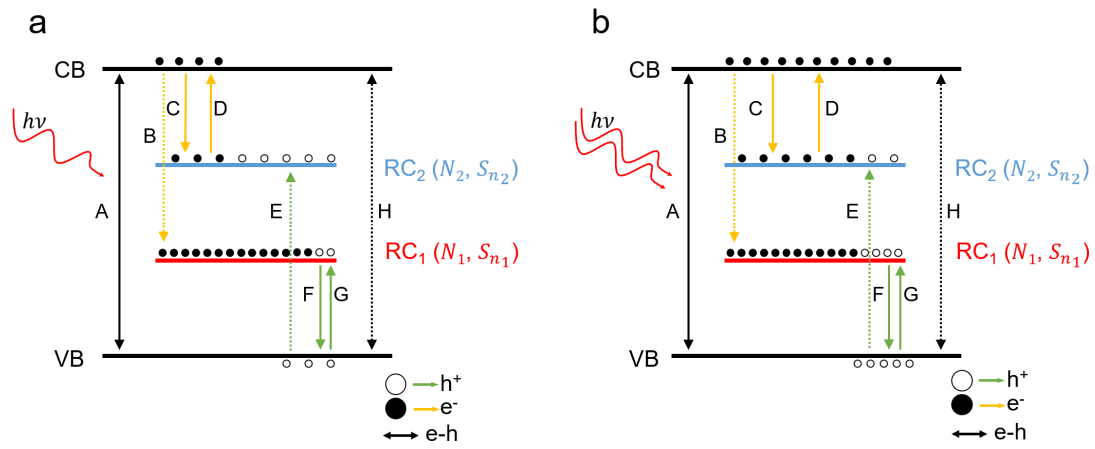


Fig. 4 | Schematic plot of the two-RC model. a, Band diagram at low illumination power. Two recombination centers (RC) are characterized by different density of states (N_i) and electron capture cross-sections (S_{n_i}). The black arrows refer to electron-hole pairs generation (A) due to the photoexcitation and recombination between free electrons and holes (H). A series of additional carrier processes coexist for both electrons (yellow arrows) and holes (green arrows), including trapping, thermal excitation, and recombination. Solid and hollow dots denote the distribution of electrons and holes on each band, respectively. At low illumination power, the RC₂ is partially filled by electrons which favors the capture and recombination processes of the photogenerated carriers. Note that the schematic plot of the energy level is not to scale. Process A is the only process from photoelectric transition while all others are electric processes. The dashed lines indicate the transitions with low probability. **b**, Band diagram at high illumination power. The major states of RC₂ become occupied which suppresses the electron trapping process. Thus, the recombination rate drops and potentially leads to superlinear power dependence of the photocurrent.

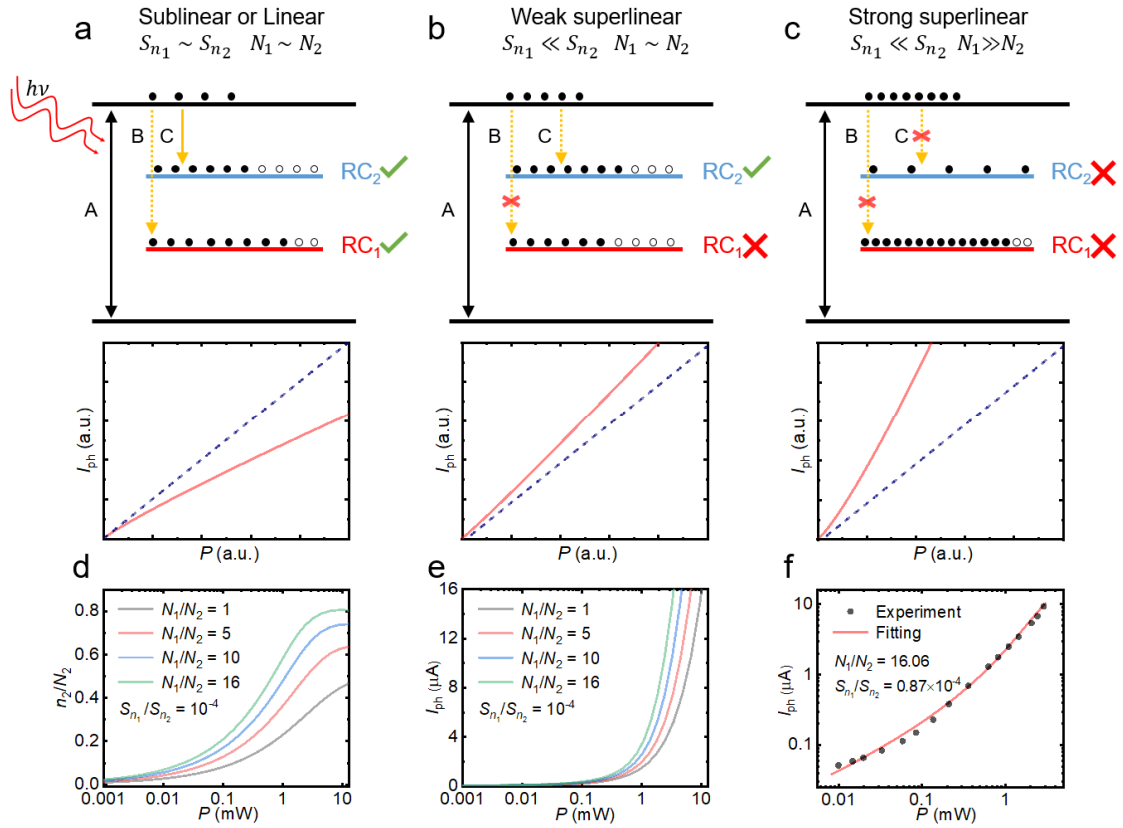


Fig. 5 | Two-RC model with different parameters and fitting to the experimental data. **a-c**, The upper panels denote the carrier distribution on the recombination centers at high illumination power. The lower panels denote the corresponding power dependence of the photocurrent. In the left panel ($S_{n1} \sim S_{n2}$, $N_1 \sim N_2$), both in-gap states work as efficient recombination centers, leading to the sublinear or linear photoresponse. In the middle panel ($S_{n1} \ll S_{n2}$, $N_1 \sim N_2$), the negligible electron capture cross-section of the lower in-gap state closes the recombination channel on the RC₁. Combined with the slow saturation of RC₂ at the high power regime, weak superlinear power dependence is achieved. In the right panel ($S_{n1} \ll S_{n2}$, $N_1 \gg N_2$), the lower density of states of upper in-gap state results in a rapid saturation which effectively closes both recombination channels and potentially leads to prominent superlinear photoresponse. **d**, The calculated occupancy ratio of RC₂ based on the two-RC model. A higher ratio of N_1/N_2 leads to a rapid saturation. **e**, The calculated power dependence of the photocurrent. The photoresponse features more prominent superlinearity with a higher N_1/N_2 ratio. **f**, The fitting to the experimental data. The two-RC model fits well with the experimental result.

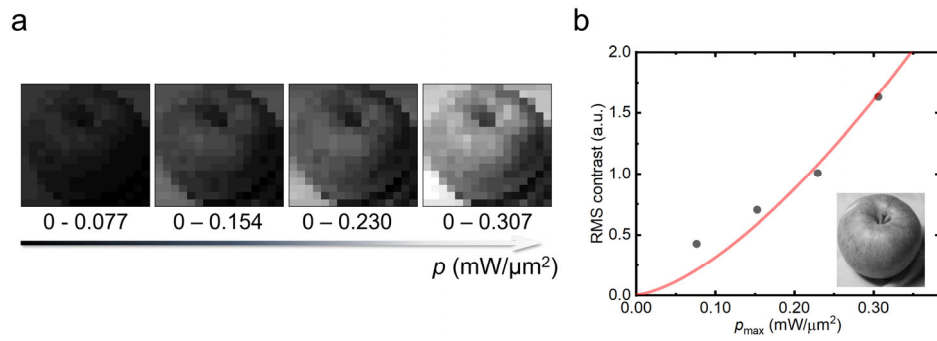


Fig. 6 | Photography by the Ta_2NiS_5 device and the image contrast. a, The images of an apple are successfully photographed which are more distinguishable with higher brightness of the target. **b,** The RMS contrast is enhanced with power following a superlinear trend. The inset is the original target.